International Communications in Heat and Mass Transfer 148 (2023) 107069

Contents lists available at ScienceDirect

International Communications in Heat and Mass Transfer

journal homepage: www.elsevier.com/locate/ichmt

Melting process investigation of a non-Newtonian phase change material containing multiwalled carbon nanotubes in a trapezoidal enclosure

Mohamed Boujelbene [a], S.A.M. Mehryan [b,*], Amira M. Hussin [c], Talal Yusaf [d,e], Mohammad Shahabadi [f], Mohammad Ghalambaz [e,*]

[a] Industrial Engineering Department, College of Engineering, University of Ha'il, Ha'il 55476, Saudi Arabia
[b] Young Researchers and Elite Club, Yasooj Branch, Islamic Azad University, Yasooj, Iran
[c] Department of Mathematics, Al-Aflaj College of Science and Humanities, Prince Sattam bin Abdulaziz University, Al-Aflaj 710-11912, Saudi Arabia
[d] School of Engineering and Technologies, Central Queensland University, Rockhampton, QLD 4701, Australia
[e] College of Engineering, Almaaqal University, Basra 61003, Iraq
[f] School of Aerospace and Mechanical Engineering, University of Oklahoma, Norman, OK 73019, United States of America

ARTICLE INFO

Keywords:
Non-Newtonian PCM
MWCNT
Enthalpy-porosity
Enclosure

ABSTRACT

This research examines the melting characteristics of nano-enhanced, non-Newtonian PCMs-multi-walled carbon nanotube (MWCNT). The process includes analyzing the impacts of various nanoparticle concentrations and trapezoidal angles by conducting simulations with these nanocomposites filled within the enclosure. The power-law shear-thinning effects are incorporated into the governing equations, which are then converted into a generalized dimensionless form using scaled parameters and solved using the finite element method. The findings underscore the significant role of enclosure geometry in influencing the melting dynamics and heat transfer process. Critical outcomes include the effect of nanoparticle concentration on the initiation of natural convection and the overall melting process, the influence of trapezoidal angle on the distribution of the molten liquid and melting dynamics, and the alteration of the melting interface shape due to nanoparticle concentration. The Nusselt number displayed intricate behavior during the melting process, changing with nanoparticle concentration. The study found that altering trapezoidal angles and nanoparticle concentrations could significantly affect melting time, with changes up to 62.5% observed. It was concluded that a trapezoidal enclosure with a slight outward angle ($\gamma = 10^{\circ}$) was most effective in reducing interference and shortening melting time, offering valuable insights for optimizing PCM design for diverse applications.

1. Introduction

The importance of effective energy storage cannot be overstated in the landscape of global energy dynamics. As our reliance on renewable energy sources continues to grow, the intermittent nature of these sources necessitates innovative solutions for storing excess energy to meet low production demand [1,2]. In this context, Phase Change Materials (PCMs) emerge as a beacon of promise. PCMs possess a remarkable ability to store and release thermal energy during phase transitions, such as melting and solidification [3]. This intrinsic characteristic allows them to absorb heat when available and release it when needed, offering a versatile and efficient means of managing thermal energy. Among the wide array of PCMs, exploring non-Newtonian formulations adds an intriguing layer of complexity. These materials exhibit viscosity changes in response to shear rates, presenting opportunities for enhanced control over heat transfer processes [4].

The effect of enclosure (cavity) shape on the melting behavior of PCMs has garnered substantial attention due to its profound implications for thermal energy storage and management. PCMs have emerged as a promising solution to address the intermittency of renewable energy sources and to enhance overall energy efficiency [5]. These materials possess the unique ability to store and release latent heat during phase transitions, offering an efficient means of capturing and releasing thermal energy. As the global demand for sustainable energy solutions intensifies, the role of PCMs in buffering supply-demand imbalances becomes increasingly crucial. Numerous investigations have been

* Corresponding authors.
E-mail addresses: alal171366244@gmail.com (S.A.M. Mehryan), t.yusaf@cqu.edu.au (T. Yusaf), m.shahabadi@ou.edu (M. Shahabadi), m.ghalambaz@gmail.com (M. Ghalambaz).

https://doi.org/10.1016/j.icheatmasstransfer.2023.107069

Available online 7 October 2023

conducted to analyze the impact of different enclosure shapes on the melting process of PCMs [6–8]. The shape of the enclosure significantly influences heat transfer mechanisms and melting characteristics. Studies have explored various enclosure geometries, including trapezoidal, hemicylindrical, rectangular, spherical, and elliptical configurations [7–11]. These investigations have revealed that the shape of the cavity plays a pivotal role in determining the melting time, heat transfer modes (conduction, convection, or both), and overall thermal performance.

Furthermore, the integration of nanoparticles into PCMs has been studied to enhance heat transfer rates during melting [6,11]. The dispersion of nanostructures within the PCM matrix modifies its thermal conductivity and alters heat transfer dynamics. Such modifications have the potential to mitigate the impact of enclosure shape on melting characteristics, leading to more efficient and rapid energy storage and release processes. An additional study examined the effect of a sinusoidal temperature along the vertical surfaces of a right-angled trapezoidal container [12]. Their findings unveiled that increasing the amplitude of sinusoidal temperature enhances the average entropy generation as well as Bejan and Nusselt number. Additionally, an investigation into mixed convection in a porous trapezoidal cavity filled with a hybrid nanofluid revealed that selecting suitable nanoparticle combinations can result in the desired heat transfer rate [13]. Meanwhile, a distinct study found that the geometric parameters of a heater in a cuboid enclosure with a trapezoidal heat source considerably influence the temperature field and fluid flow [14].

Several recent studies have investigated the phase change heat transfer of PCMs [15,16]. One study delved into free convection melting in both 3D and 2D chambers [17], developing proper heat removal systems for electronic components. The authors reported that the melting was intense in the 3D case, while the rate of heat transfer was better in the 2D scenario at the heater. In a separate pore-scale numerical investigation, the melting process of a composite PCM-metal foam with Kelvin cells was studied [18]. The results demonstrated that the metal foam Kelvin cells decreased the melting time and increased the overall rate of heat transfer. Interestingly, as the cell per length number increased, the melting time for smaller cavities shortened.

Another contribution of the present research is modeling PCM's behavior in non-Newtonian conditions, which poses a distinct challenge, considering the complexity of phase change and the involvement of nanoparticles. There are few research studies considering phase change heat transfer with non-Newtonian effects. Considering the nanoparticles-enhanced phase change material (NEPCM), Zhuang et al. [19] shed light on the transition from non-Newtonian to Newtonian fluid behavior models during the melting process. The thermal conductivity of pure paraffin was augmented by the inclusion of nanoparticles. Using heat source terms, Ghalambaz et al. [20] examined the phase change process of non-Newtonian magnetohydrodynamic and ferrohydrodynamic PCMs. Here, researchers found that alterations in the Power-law index and Hartman number play a crucial role in determining the melting rate and normalized melt volume fraction.

Continuing in a similar vein, another study [21] utilizes a computational approach to simulate the non-Newtonian melting process using a 2D enthalpy-based lattice Boltzmann method. This research pinpoints an association between the flow behavior index, the average Nusselt number at the heated surface, and the melting rate. Khan et al. [22] scrutinized non-Newtonian and non-isothermal fluid dynamics between contracting channels. The outcomes highlight that the Hartman number and thermal diffusivity variations profoundly impact the capillary area and concentration rate. Lastly, [23] numerically probed phase change heat transfer in a latent heat TES system filled with a non-Newtonian PCM. Findings from this research suggest that the Rayleigh number, nanoparticle fraction, and internal heater size significantly influence the melting performance of the composited PCM. Haddad et al. [24] focused on optimizing the melting performance of a thermal energy storage (TES) system using a combination of heat transfer enhancement approaches. The study introduced new design configurations aimed at enhancing the system's efficiency. The findings indicated that a hybrid approach, combining an optimum porosity metal foam layer with the use of nanoparticles, outperformed the individual utilization of each technique, resulting in improved overall efficiency.

Morphing shapes optimization in alignment with Bejan's Constructal theory has been explored across diverse applications. In one study, the constructal design was used to optimize T-shaped fins on a trapezoidal basement for heat removal, employing exhaustive search and genetic algorithms [25]. Another investigation applied constructal design to enhance heat transfer in a lid-driven cavity involving an isothermal block, emphasizing geometry's influence on performance [26]. Additionally, the integration of differential evolution and constructal design optimized double Y-shaped cooling cavities within heat-generating walls [27]. In microfluidics, the synergy of construction design, response surface optimization, and CFD led to advanced passive micromixer designs with multiple obstacles [28].

The exploration and development of novel materials have been instrumental in technological advancements and the evolution of various industries. The field of nanotechnology, in particular, has garnered significant attention due to its potential to revolutionize numerous areas ranging from electronics to medicine and energy conservation to environmental science. Among the plethora of nanomaterials, phase change materials (PCMs) embedded with multi-walled carbon nanotube (MWCNT) particles have proven to be significantly promising [29,30]. These unique materials, characterized by their capacity to absorb, store, and release considerable amounts of energy during their phase transitions, have opened new possibilities for sustainable energy storage and management [31,32].

However, the full potential of these materials cannot be realized without an in-depth understanding of their behavior within different confines. One such confinement is a trapezoidal enclosure. The trapezoidal shape offers an intriguing geometric variable for evaluating how confinement geometry impacts the PCM's thermal behavior. The study of natural convection in trapezoidal enclosures has attracted considerable attention in various disciplines, such as solar collectors, nuclear energy, heat exchangers, and electronic devices, due to its extensive applications. Multiple studies have focused on understanding the complexities of heat transfer within these distinct geometries.

A different study focused on the numerical analysis of the laminar flow of Ag-Al_2O_3/H_2O hybrid nanofluid in a modified trapezoidal porous enclosure [33]. Their findings recommended reducing the Hartmann number for enhanced thermal transfer, suggesting the potential benefits of tweaking the trapezoid's geometrical features for prolonged thermal efficiency. Another research investigated the transportation of energy through natural convection, which was propelled by the combined influences of buoyancy caused by thermal and solute diffusion within a trapezoidal container [34]. The study further bolstered the body of existing research by validating their results against previous studies.

The realm of phase change heat transfer involving non-Newtonian effects stands as a pivotal yet underexplored subject in current literature. Similarly, the realm of natural convection heat transfer within trapezoidal enclosures has been gaining prominence due to its relevance in both structural and thermal design applications. Surprisingly, the nuanced intersection of phase change heat transfer with non-Newtonian effects within a trapezoidal cavity has remained largely untrodden. To fill this significant void, this study takes up the mantle of investigating the heat transfer dynamics of non-Newtonian NEPCMs within a trapezoidal enclosure. In delving into this uncharted territory, this pioneering research aims to unravel the complexities inherent in phase change heat transfer involving non-Newtonian fluids within the distinct confines of a trapezoidal enclosure. The anticipated outcome is a compendium of invaluable insights that will not only enrich the understanding of such intricate heat transfer phenomena but also furnish essential knowledge for the design and optimization of TES systems leveraging the potential of PCMs.

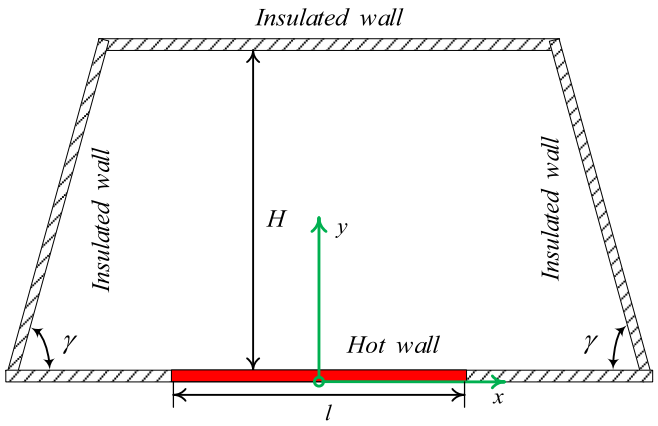

Fig. 1. Illustrative depiction of the physics involved in the problem.

Table 1
Non-Newtonian indexes of the liquid nano-PCM and the thermal conductivities of the solid and liquid phases for different volume fractions of MWCNT particles [35].

Concentration (φ)	0.0%	0.05%	0.1%	0.3%	0.5%
Power law index ($n_{com,l}$)	0.93	0.78	0.71	0.65	0.56
Consistency ($m_{com,l}$) [mPa.s^n]	0.0926	0.127	0.141	0.203	0.246
Thermal conductivity of solid phase ($k_{com,s}$) [W/m.K]	0.23	0.268	0.307	0.344	0.375
Thermal conductivity of liquid phase ($k_{com,l}$) [W/m.K]	0.174	0.183	0.200	0.203	0.208

Table 2
Thermo-physical virtues of the pure PCM and MWCNTs nano-sized particles.

Virtues	Pure PCM	MWCNT
Density (liquid/ solid) [kg/m^3]	1050/ 1111	1600
Melting latent heat [kJ/kg]	180	–
Coefficient of thermal expansion [1/K]	1.e-3	1.9e-5
Sensible heat capacity (liquid/ solid) [J/kg.K]	2100/ 1710	796

1.1. Physic of the problem

The research under consideration focuses on a 2D trapezoidal cavity filled with nanocomposites based on PCM OM08-MWCNTs, as illustrated in Fig. 1. The cavity walls are assumed to be completely insulated, except for a specific section of the bottom wall where heat is transferred to the nanocomposites. PCM-filled channel enclosures, available in diverse geometries, find utility within TES units. The heat transfer medium navigates along the channel peripheries, interchanging thermal energy with the enclosure walls, resulting in PCM melting. To accommodate the channel arrangement, mechanical supports are essential, inevitably exposing sections of the wall for heat exchange with the transfer medium. As a result, a localized region of the wall experiences heating. The nanocomposites based on melted PCM OM08-MWCNTs exhibit power law non-Newtonian fluid behavior, which is attributed to the presence of nanoparticles in the PCM (see Table 1). It is assumed that there is no change in the mixture volume during the phase change flow. The implemented model simulates the buoyancy force by utilizing the Boussinesq approximation. The conservative equations for this study are as follows, taking into account the assumptions of unsteady, incompressible, and non-Newtonian flow.

Continuity equation:

$$\rho_{com}\nabla^*\cdot\vec{u}=0 \tag{1}$$

Momentum equation:

Table 3
Values of MVF for different mesh sizes at $Fo = 0.5$ and $Fo = 1.0$.

Cases	1	2	3	4
Grid size	75 × 75	100 × 100	125 × 125	150 × 150
MVF ($Fo = 0.5$)	0.36118	0.36058	0.36024	0.36017
Err^*	0.166 (%)	–	0.094 (%)	0.114 (%)
MVF ($Fo = 1.0$)	0.7722	0.7730	0.7732	0.7743
Err^*	0.104 (%)	–	0.026 (%)	0.168 (%)

* $Err = |\frac{MVF_i - MVF_2}{MVF_2}| \times 100$, which i is the case number.

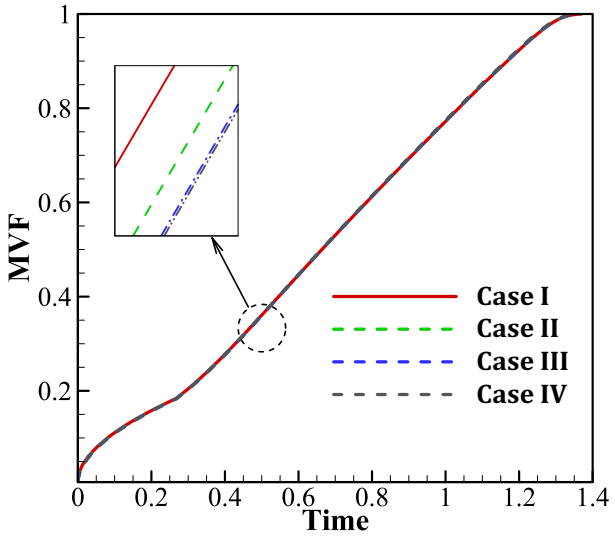

Fig. 2. Melted volume fraction (MVF) for different grids.

$$\rho_{com,l}\left[\frac{\partial\vec{u}}{\partial t}+(\vec{u}\cdot\nabla^*)\vec{u}\right]=\nabla^*\cdot\left[-pI+\mu_{com,l}\left(\nabla^*\vec{u}+(\nabla^*\vec{u})^{tr}\right)\right]+\vec{f}_b+\vec{f}_m \tag{2}$$

in which

$$\mu_{com,l}(\dot{\gamma})=m_{com,l}\dot{\gamma}^{n_{com,l}-1}\left|\begin{cases}\dot{\gamma}=max\left(\sqrt{[D^{'}]:[D^{'}]},\dot{\gamma}_{min}\right)\\ 2D^{'}=\left(\nabla\vec{u}+(\nabla\vec{u})^{tr}\right)\end{cases}\right.$$

$$\vec{f}_b=f_{b,x}i+f_{b,y}j\left|\begin{array}{c}f_{b,x}=0\\ f_{b,y}=(\rho\beta)_{com,l}g\left(T-T_{fu}\right)\end{array}\right.$$

$$\vec{f}_m=f_{m,x}i+f_{m,y}j\left|\begin{array}{l}f_{m,x}=a_{mush}\dfrac{(1-\Upsilon)^2}{\Upsilon^3+e}u,\\ f_{m,y}=a_{mush}\dfrac{(1-\Upsilon)^2}{\Upsilon^3+e}v\end{array}\right. \tag{3}$$

where a_{mush} is mthe ushy zone parameter ($a_{mush}=10^5$), e is a numerical constant ($e=10^{-3}$), and Υ is defined as follows:

$$\Upsilon(T)=\begin{cases}0 & T\le T_{fu}-0.5\Delta T_{fu}\\ \dfrac{2(T-T_{fu})+\Delta T_{fu}}{2\Delta T_{fu}} & T_{fu}-0.5\Delta T_{fu}<T<T_{fu}+0.5\Delta T_{fu}\\ 1 & T\ge T_{fu}+0.5\Delta T_{fu}\end{cases} \tag{4-a}$$

Energy balance equation:

$$(\rho C_p)_{com}\frac{\partial T}{\partial t}+(\rho C_p)_{com}\vec{u}\cdot\nabla^*T=\nabla^*\cdot(k_{com}\nabla^*T)-(\rho L_{sf})_{com}\frac{\partial\Upsilon}{\partial t} \tag{4-b}$$

The boundary conditions imposed in the mathematical form are:

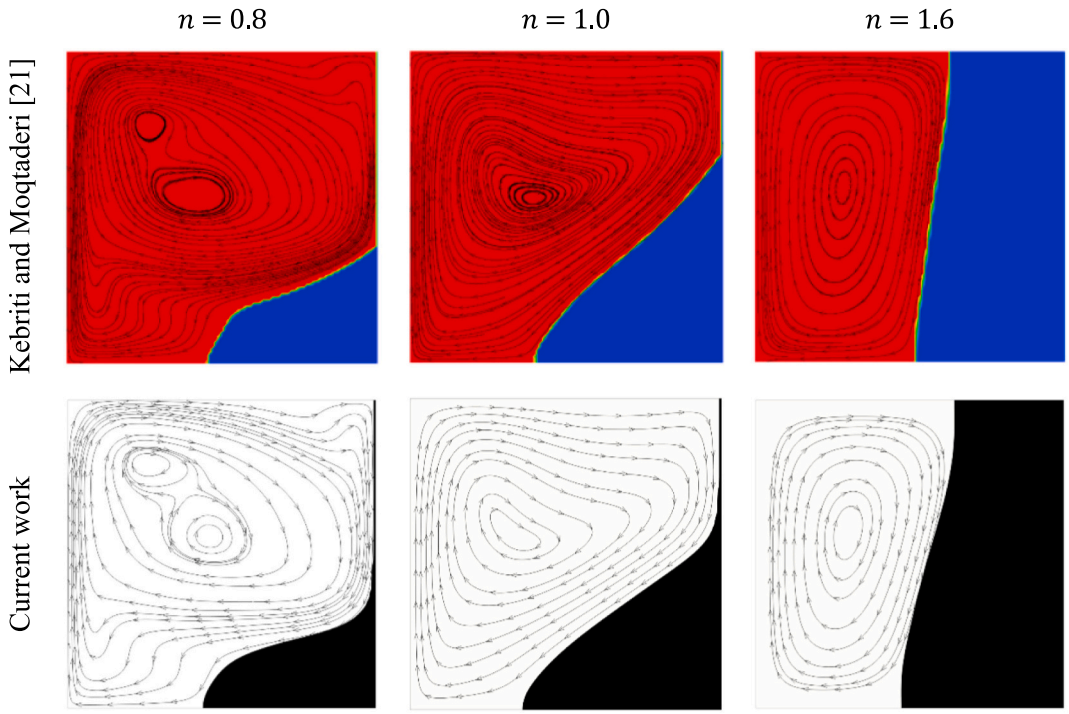

Fig. 3. A comparison was made between the results obtained in [21] and the findings of the current study.

Table 4
MVF Values for different power-law indexes of the PCM at $Fo \times Ste = 0.5$.

n	0.8	1.0	1.4
MVF (Kebriti and Moqtaderi [21])	0.87	0.79	0.57
MVF (Current study)	0.84	0.77	0.56
Err^*	3.4 (%)	2.5 (%)	1.8 (%)

* $Err = |\frac{MVF_K - MVF_C}{MVF_K}| \times 100$, which K and C denote the normalized melted volume fraction represented by Kebriti and Moqtaderi [21], and current work.

The right boundary:

$$\frac{\partial T(x,y,t)}{\partial n} = 0, u(x,y,t) = v(x,y,t) = 0 \quad (5\text{-a})$$

The upper boundary:

$$\frac{\partial T(x,H,t)}{\partial y} = 0, u(x,H,t) = v(x,H,t) = 0 \quad (5\text{-b})$$

The left boundary:

$$\frac{\partial T(x,y,t)}{\partial n} = 0, u(x,y,t) = v(x,y,t) = 0 \quad (5\text{-c})$$

The bottom wall:

(a) Insulated sections

$$\frac{\partial T(x,0,t)}{\partial y} = 0, u(x,0,t) = \mathrm{v}(x,0,t) = 0 \, for \, x < -\frac{l}{2} \, and \, \frac{l}{2} < x \quad (5\text{-d})$$

(b) Hot wall

$$T(x,0,t) = T_h, u(x,0,t) = v(x,0,t) = 0 \, for \, \frac{-l}{2} \le x \le \frac{l}{2} \quad (5\text{-e})$$

The entire cavity experiences the initial condition as follows:

$$T(x,y,0) = T_0, u(x,y,0) = v(x,y,0) = 0 \quad (5\text{-f})$$

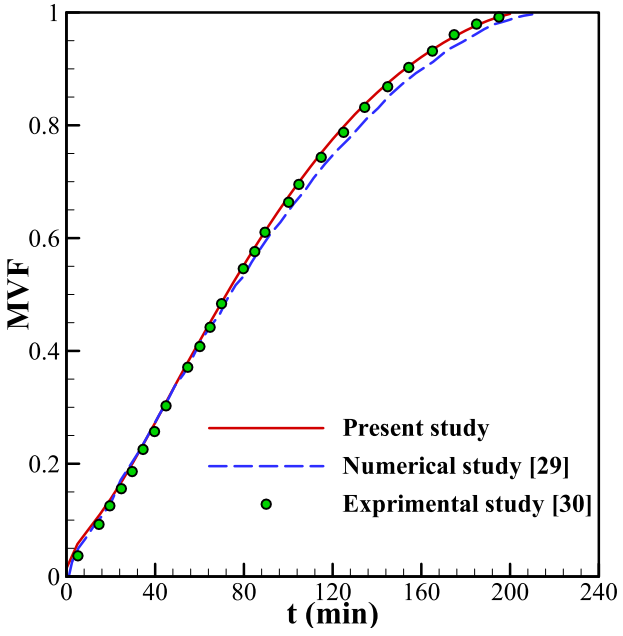

Fig. 4. The results of the current research were compared with the findings of Kamkari et al. [42] and Kamkari and Amlashi [43] for further analysis and comparison.

The investigation of PCM OM08-MWCNTs based nanocomposites has been limited, and there is currently no established model for determining its thermophysical parameters. Therefore, the values for key parameters, such as thermal conductivity and dynamic viscosity of this non-Newtonian nano-PCM material, were derived from the experimental research conducted by Kim et al. [35]. This research examined the impact of varying nanoparticle concentrations on PCM's solid and liquid phases. The findings suggest that the conductivity and dynamic viscosity of the PCM OM08-MWCNTs nanocomposites increased with an

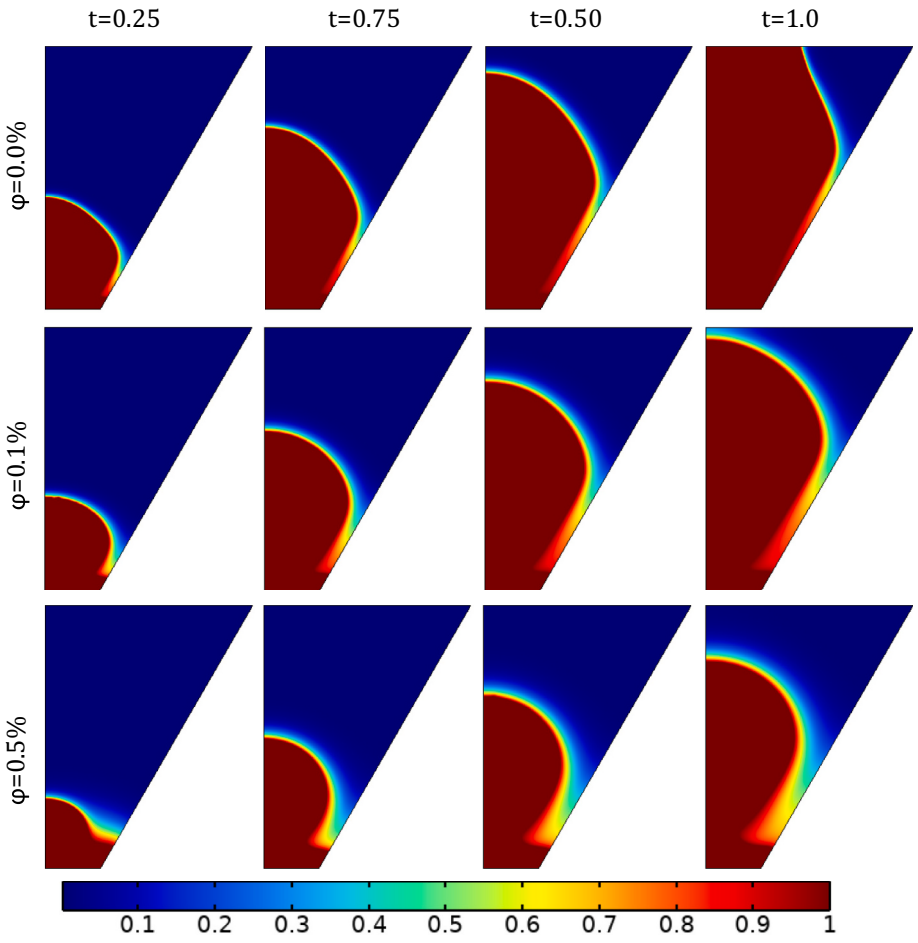

Fig. 5. Melting fields for different values of φ at $\gamma = 30^{\circ}$.

increase in the nanoparticle fraction. Additionally, this investigation was able to approximate the power-law index and consistency parameter of the PCM accurately across a range of MWCNT concentrations. Table 2 includes values for the power law index, consistency, and thermal conductivities of the solid and liquid phases of the NCPCM, calculated for various nanoparticle concentrations. Table 3 presents a comprehensive list of the thermophysical virtues of pure PCM and MWCNTs. The remaining parameters of the nanocomposite were determined as follows:

Density of the nano-PCM:

$$\rho_{com,l} = (1-\varphi)\rho_{bPCM,l} + \varphi\rho_{na} \tag{6-a}$$

$$\rho_{com,s} = (1-\varphi)\rho_{bPCM,s} + \varphi\rho_{na} \tag{6-b}$$

Heat capacity of nano-PCM:

$$\left(\rho C_p\right)_{com,l} = \varphi\left(\rho C_p\right)_{np} + (1-\varphi)\left(\rho C_p\right)_{bPCM,l} \tag{7-a}$$

$$\left(\rho C_p\right)_{com,s} = \varphi\left(\rho C_p\right)_{np} + (1-\varphi)\left(\rho C_p\right)_{bPCM,s} \tag{7-b}$$

The volumetric coefficient of thermal expansion of the liquid phase:

$$(\rho\beta)_{com,l} = (1-\varphi)(\rho\beta)_{bPCM,l} + \varphi(\rho\beta)_{np} \tag{8}$$

Latent heat of the nano-PCM:

$$\left(\rho L_{sf}\right)_{com,l} = (1-\varphi)\left(\rho L_{sf}\right)_{bPCM} \tag{9}$$

To convert the governing equations to non-dimensional coordinates, the following dimensionless parameters were utilized:

$$X = \frac{x}{H}, Y = \frac{y}{H}, L = \frac{l}{H}, U = \frac{uH}{\alpha_{bPCM,l}}, V = \frac{vH}{\alpha_{bPCM,l}},$$

$$\theta = \frac{T - T_{fu}}{T_h - T_{fu}}, P = \frac{H^2 p}{\rho_{bPCM,l}\alpha_{bPCM,l}^2}, Fo = \frac{t\alpha_{bPCM,l}}{H^2} \tag{10}$$

The equations, expressed in non-dimensional form, derived from the aforementioned correlations, are as follows:

$$\nabla\cdot\vec{U} = 0 \tag{11}$$

$$\frac{\partial\vec{U}}{\partial Fo} + \left(\vec{U}\cdot\nabla\right)\vec{U} = \nabla\cdot\left[-PI\frac{\rho_{bPCM,l}}{\rho_{com,l}} + Pr\left[\frac{m_{com,l}}{m_{bPCM,l}}\frac{\alpha_{bPCM,l}^{n_{com,l}}}{\alpha_{bPCM,l}^{n_{bPCM,l}}}\frac{L^{2n_{bPCM,l}}}{L^{2n_{com,l}}}\right]\dot{G}^{n_{com,l}-1}\left(\nabla\vec{U} + \left(\nabla\vec{U}\right)^{tr}\right]\right] + \vec{F}_b + \vec{F}_m \tag{12}$$

in which

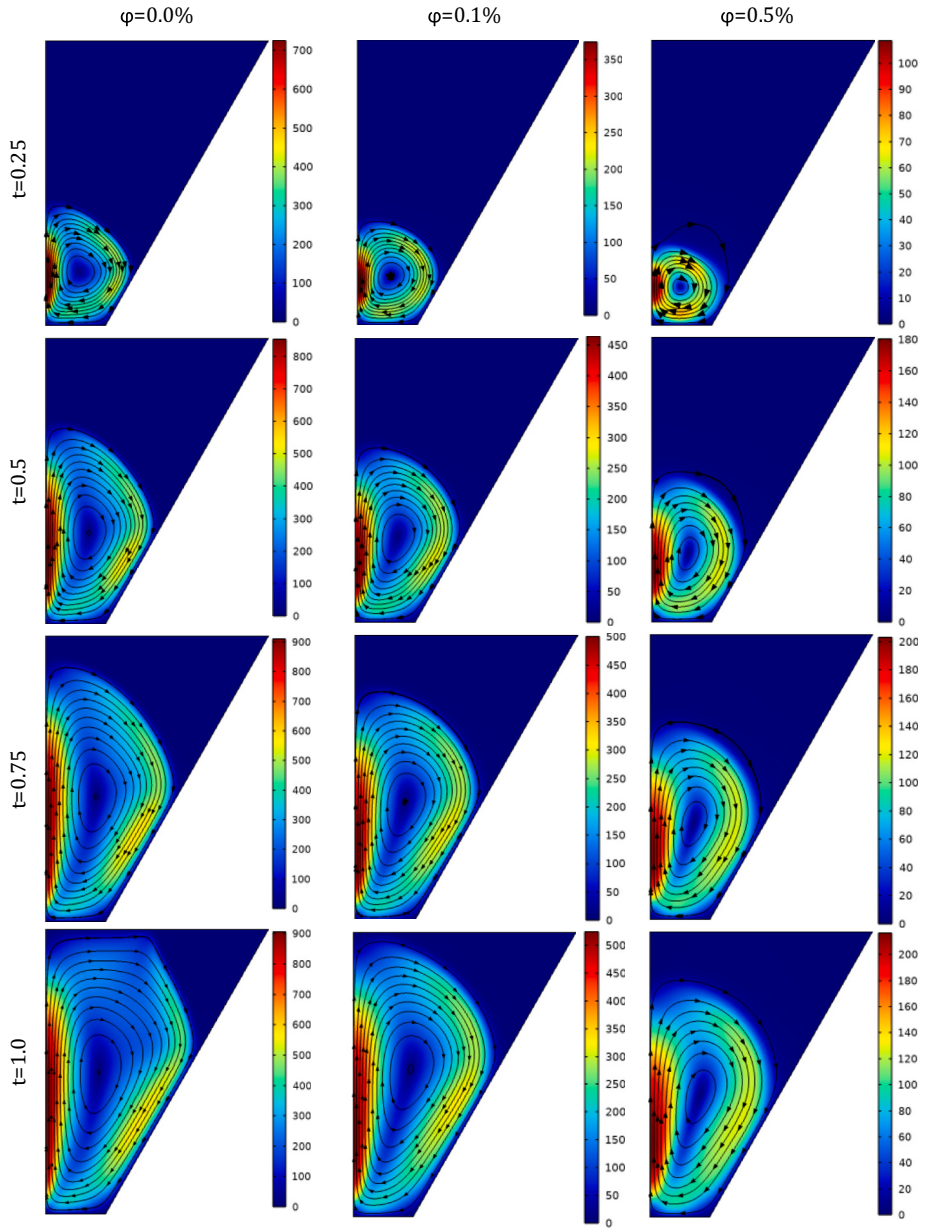

Fig. 6. Velocity magnitude and streamlines for different values of φ over time at $\gamma = 30°$.

$$\overrightarrow{F}_b = F_{b,X}i + F_{b,Y}j \;\Big|\; F_{b,X} = 0, F_{b,Y} = \frac{\beta_{com,l}}{\beta_{bPCM,l}} RaPr\theta$$

$$\overrightarrow{F}_m = F_{m,x}i + F_{m,y}j \;\Big|\; \begin{array}{l} F_{m,x} = A_{mush}\dfrac{\rho_{bPCM,l}}{\rho_{com,l}}\dfrac{(1-\Upsilon)^2}{\Upsilon^3+e}U, \\ F_{m,y} = A_{mush}\dfrac{\rho_{bPCM,l}}{\rho_{com,l}}\dfrac{(1-\Upsilon)^2}{\Upsilon^3+e}V \end{array}$$

$$\dot{G} = max\left(\sqrt{[D]:[D]}, \dot{G}_{min}\right) \;\Big|\; 2D = \left(\nabla\overrightarrow{U} + \left(\nabla\overrightarrow{U}\right)^{tr}\right) \tag{13}$$

$$\frac{\partial\theta}{\partial Fo} + \overrightarrow{U}\cdot\nabla\theta = \frac{(\rho C_p)_{bPCM,l}}{(\rho C_p)_{com}}\left(\nabla\cdot\left(\frac{k_{com}}{k_{bPCM,l}}\nabla\theta\right)\right) - (1-\varphi)\frac{(\rho C_p)_{bPCM,l}}{(\rho C_p)_{com}}\frac{1}{Ste}\frac{\partial\Upsilon}{\partial Fo} \tag{14}$$

where

$$k_{com} = (1-\Upsilon)k_{com,s} + \Upsilon k_{com,l} \tag{15}$$

$$(\rho C_p)_{com} = (1-\Upsilon)(\rho C_p)_{com,s} + \Upsilon(\rho C_p)_{com,l} \tag{16}$$

The Prandtl number (*Pr*) and Rayleigh number (*Ra*) are expressed in the following manner:

$$Pr = \frac{m_{bPCM,l}}{\rho_{bPCM,l}}\frac{\alpha_{bPCM,l}^{n_{bPCM,l}-2}}{H^{2n_{bPCM,l}-2}}, Ra = \frac{\rho_{bPCM,l}g\beta_{bPCM,l}\Delta TH^{2n_{bPCM,l}+1}}{m_{bPCM,l}\alpha_{bPCM,l}^{n_{bPCM,l}}}, A_{mush} = \frac{a_{mush}H^2}{\rho_{bPCM,l}\alpha_{bPCM,l}} \tag{17}$$

The definition of the Stefan number (*Ste*) is as follows:

$$Ste = \frac{C_{p,bPCM,l}\Delta T}{L_{sf,bPCM}} \tag{18}$$

The thermal and hydrodynamic conditions of the walls in

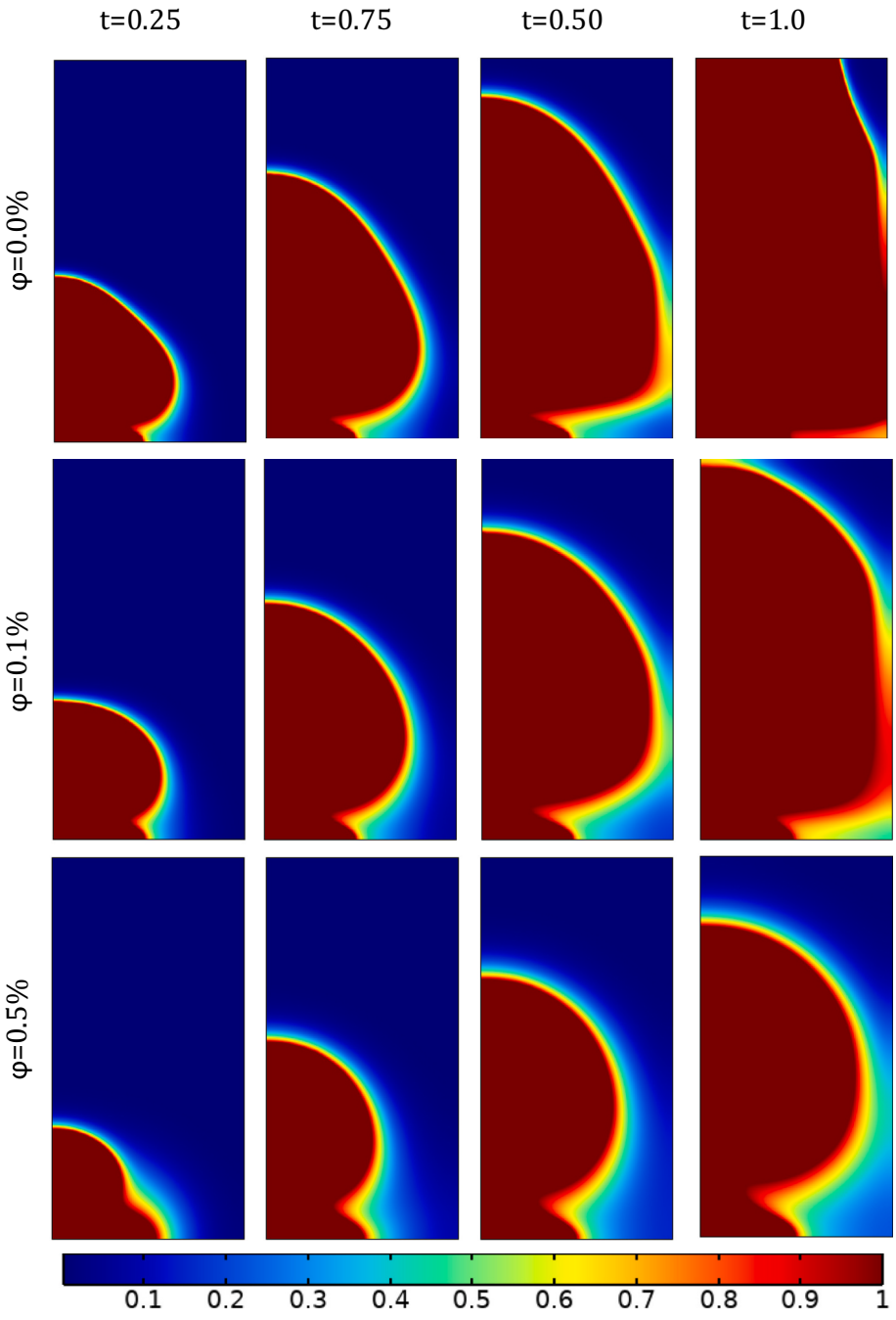

Fig. 7. Melting fields for different values of φ at $\gamma = 0.0°$.

dimensionless space can be described as follows:

The right boundary:

$$\frac{\partial\theta(X,Y,Fo)}{\partial N} = 0, U(X,Y,Fo) = V(X,Y,Fo) = 0 \quad \text{(19-a)}$$

The upper boundary:

$$\frac{\partial\theta(X,1,Fo)}{\partial N} = 0, U(X,1,Fo) = V(X,1,Fo) = 0 \quad \text{(19-b)}$$

The left boundary:

$$\frac{\partial\theta(X,Y,Fo)}{\partial N} = 0, U(X,Y,Fo) = V(X,Y,Fo) = 0 \quad \text{(19-c)}$$

The bottom wall:

(a) Insulated sections

$$\frac{\partial\theta(X,0,Fo)}{\partial Y} = 0, U(X,0,Fo) = V(X,0,Fo) = 0 \; for \; X < -\frac{L}{2} \; and \; \frac{L}{2} < X \quad \text{(19-d)}$$

(b) Hot wall

$$\theta(X,0,Fo) = 1, U(X,0,Fo) = V(X,0,Fo) = 0 \; for \; \frac{-L}{2} \le X \le \frac{L}{2} \quad \text{(19-e)}$$

The entire cavity experiences the initial condition as follows:

$$\theta(X,Y,0) = \theta_0, U(X,Y,0) = V(X,Y,0) = 0 \quad \text{(19-f)}$$

In this study, the key parameters of concern are the proportion of melted material within the cavity and the Nusselt number at the heated

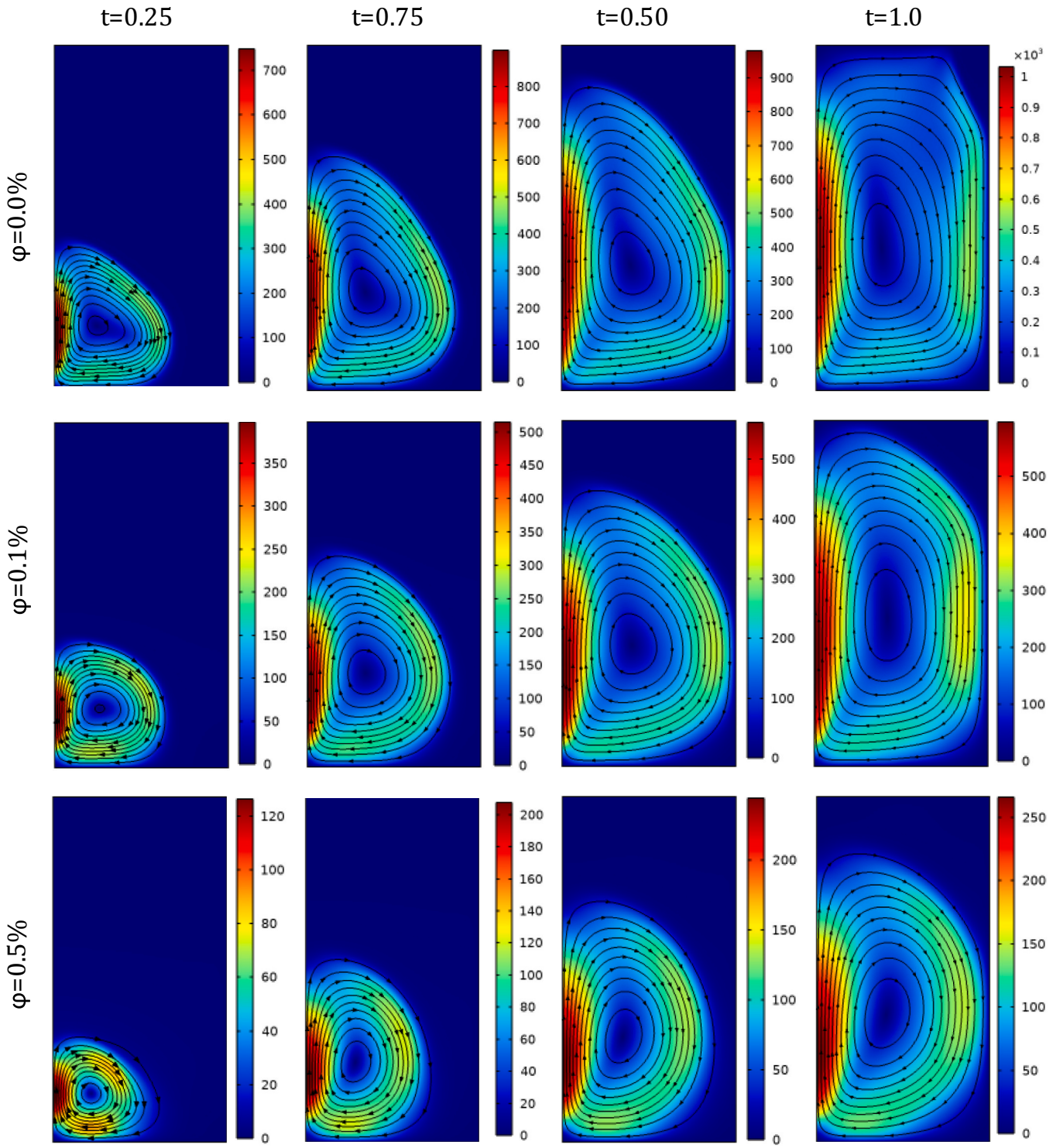

Fig. 8. Velocity magnitude and streamlines for different values of φ over time at $\gamma = 0.0°$.

boundary. The volume fraction of the melt is scaled by the total volume of the cavity, resulting in the introduction of a normalized measure for the melt volume fraction.

$$MVF = \frac{\int_{\forall} \Upsilon(\theta) d\forall}{\int_{\forall} d\forall} \tag{20}$$

where $\forall$ is the surface of trepizodal enclosure and $d\forall$ represents an individual element. The following expression is obtained when considering the energy balancing of the control surface located on the hot boundary.

$$h(T - T_c) = -k_{com} \frac{\partial T}{\partial y}\Big)_{y=0, x_1 \le x \le x_2} \tag{21}$$

where x_1 and x_2 are equal to $-l/2$ and $l/2$, respectively. The establishment of the local Nusselt number is accomplished by transferring the relation above into dimensionless space:

$$Nu_l = \frac{hH}{k_{bPCM,l}} = \frac{k_{com}}{k_{bPCM,l}} \frac{\partial \theta}{\partial Y}\Big|_{Y=0, X_1 \le X \le X_2} \tag{22}$$

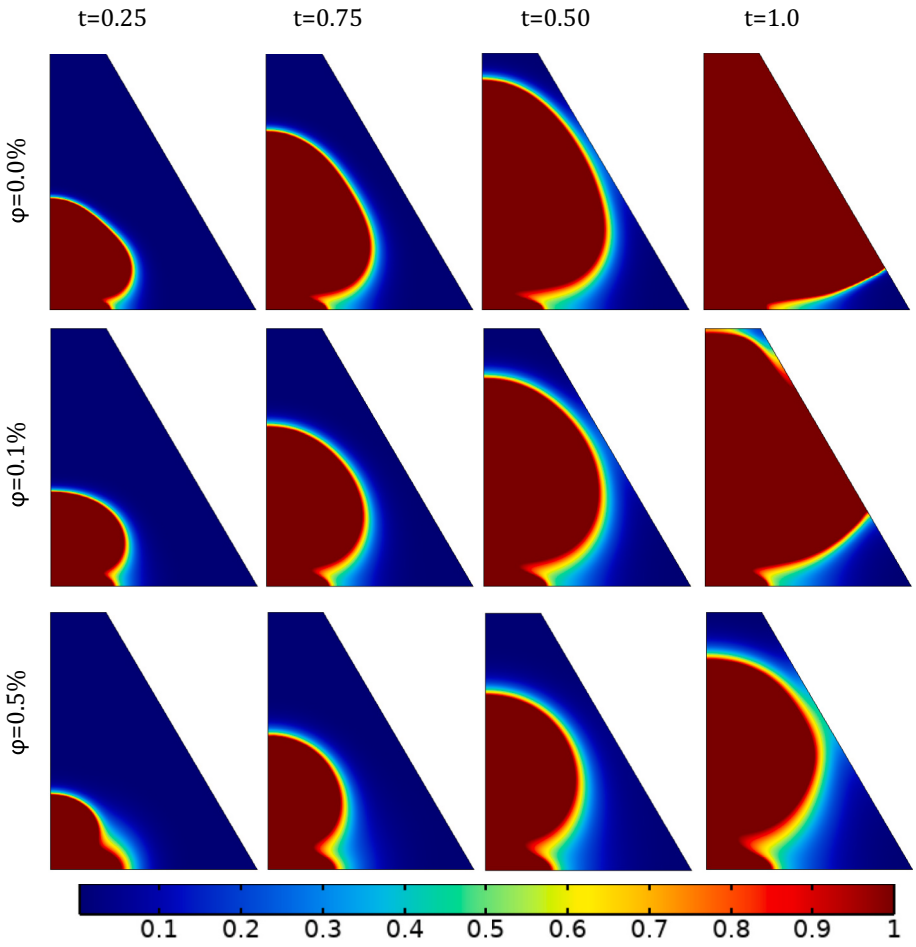

Fig. 9. Melting fields for different values of φ over time at $\gamma = -30°$.

Finally, the average Nusselt number, i.e. Nu_{avg}, is defined as:

$$Nu_{avg} = \frac{\int_{X_1}^{X_2} Nu_l dX}{X_2 - X_1} \tag{23}$$

where X_1 and X_2 are equal to $-L/2$ and $L/2$, respectively.

2. Numerical approach, grid test, and model validation

Galerkin finite element approach is utilized to solve the governing partial differential equations along with the boundary conditions. In this approach, the domain of interest is first discretized into a set of smaller subdomains or elements, and a piecewise polynomial approximation of the solution is constructed over each element. The method used for discretizing the domain in order to solve the momentum equations and compute the dependent variables, i.e. velocity components and pressure, employs a P1 + P1 discretization mode. In the context of P1 + P1 discretization, it signifies the utilization of linear elements for both the velocity components and the pressure field. The default element order for the laminar and turbulent flows is P1 + P1. Linear elements are preferred because they are computationally cheaper than higher-order elements and tend to introduce fewer spurious oscillations, enhancing numerical robustness. Also, discretization of the energy equation to calculate the temperature variable applies a first-order, linear discretization [36]. The Galerkin approach involves multiplying the governing equations by a test function and integrating them over the domain. The test function is chosen to be orthogonal to the basis functions used for the approximation, which ensures that the resulting system of equations is well-posed and has a unique solution. The Galerkin approach leads to a system of algebraic equations that can be solved numerically using standard techniques [37]. The current investigation employs a technique to regulate the time-step, namely the free step Backward Differentiation Formula (BDF) method, along with an automated timestep selection of first-second order [38]. To examine the trend of residual equations, a Newton method has been employed utilizing the PARallel DIrect SOlver (PARDISO) solver [39–41], with a Newtonian damping factor of 0.8 and a residual error of O(10^{-5}).

The process of conducting a grid independence test holds significant importance in ensuring the precision and accuracy of simulations and solutions. A structured mesh has been provided for the domain study, and MVF of PCM OM08-MWCNTs based nanocomposites during the time-steps has been considered as the case study. So, four different grid cases with 75×75, 100×100, 125×125, and 150×150 elements have been provided to examine the behavior of each one on the MVF in different time snaps. As illustrated in Fig. 2, it is observed that there is no such significant difference among the four cases. Moreover, Table 3 shows that the change of mesh size for case 2 provides just 0.114% and 0.168% error for $Fo = 0.5$ and $Fo = 1.0$, compared to the finest mesh. Thus, as a balance between the computational cost and accuracy, the mesh of case 2 was adopted for the computations.

To verify the precision of the numerical model proposed in this paper, several comparisons were performed with previously published studies in the literature [21,42,43]. The effectiveness of the used computational code can be confirmed through validation utilizing the numerical data provided by Kebriti and Moqtaderi [21]. This data specifically pertained to the melting process of the buoyancy-driven flow of a power-law PCM within a differentially heated enclosure. Fig. 3 demonstrates a remarkable concurrence between the melt flow structure and

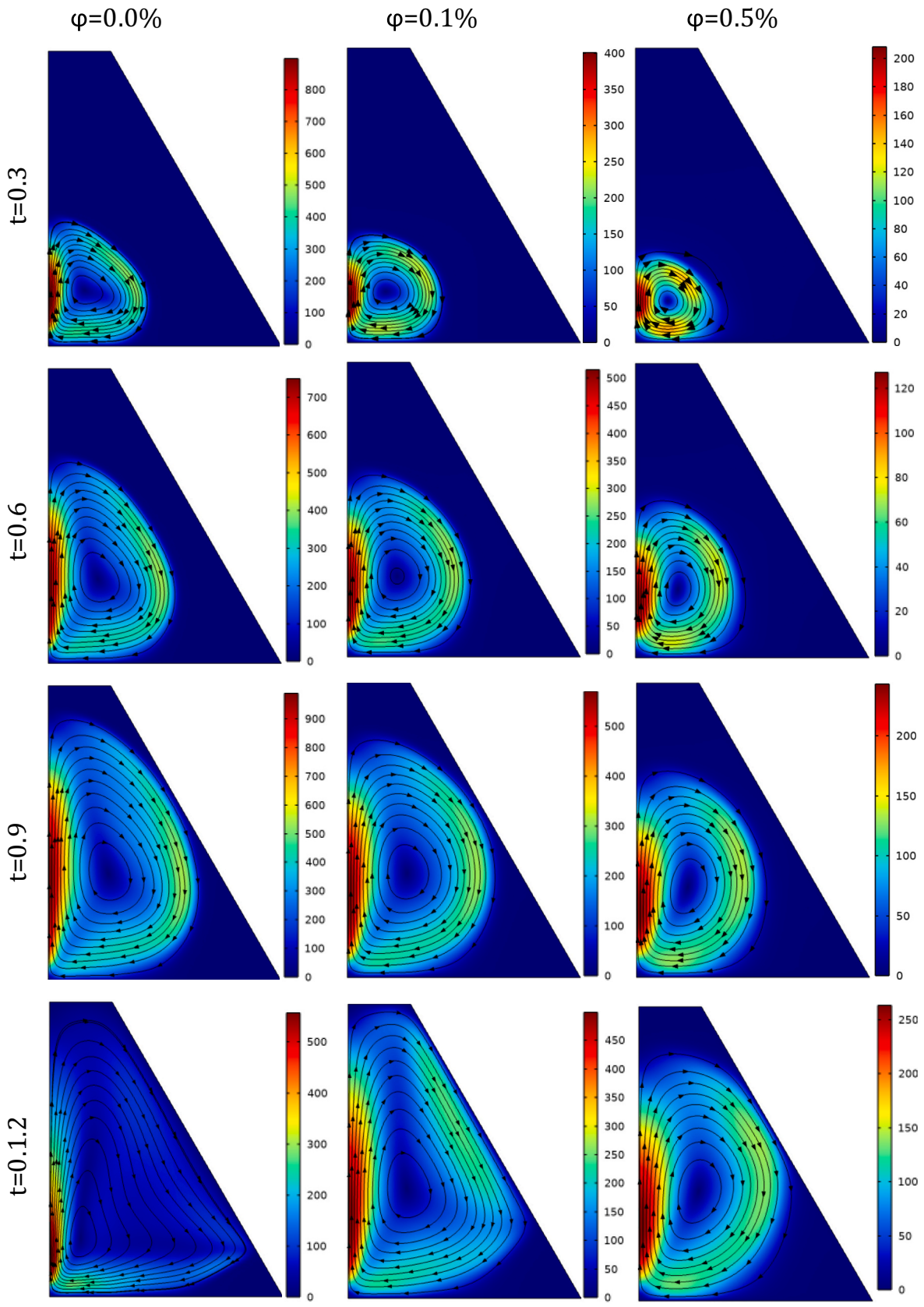

Fig. 10. Velocity magnitude and streamlines for different values of φ over time at $\gamma = -30°$.

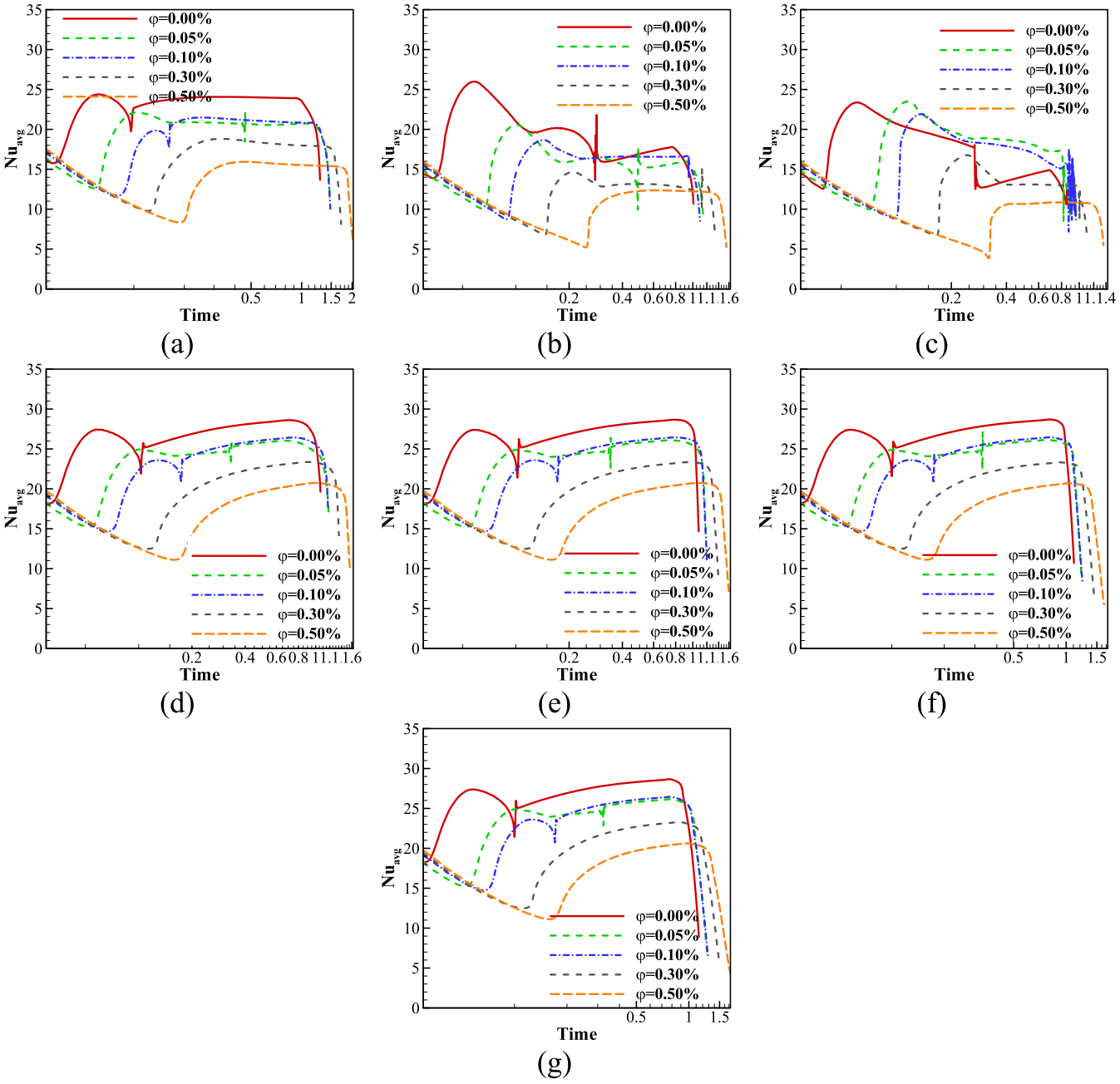

Fig. 11. Average Nusselt number for different values of φ at (a) $\gamma = +30°$, (b) $\gamma = +20°$, (c) $\gamma = +10°$, (d) $\gamma = 0.0°$, (e) $\gamma = -10°$, (f) $\gamma = -20°$, and (g) $\gamma = -30°$.

melting volume across various power-law indexes of the PCM (n). Table 4 displays the MVF values for various power-law indexes of the PCM, and it is noticeable that there is only a marginal distinction between the MVF values found in the investigation of Kebriti and Moqtaderi [21] and those in the current study.

To ensure the precision and accuracy of the simulations, the results obtained from the present model were further validated by comparing them to prior research (Fig. 4). Specifically, the findings were compared to the studies conducted by Kamkari et al. [42] and Kamkari and Amlashi [43]. These studies focused on investigating the melting behavior of lauric acid within an enclosure featuring a vertical hot wall maintained at a temperature of 70 °C. The dimensions of the container used in their experiments were 50 mm in width and 12 cm in height. By conducting the comparison, it was observed that the calculations carried out in the present study exhibit a satisfactory level of agreement with both experimental and numerical literature endeavors. This comparison plays a crucial role in affirming the accuracy and reliability of the model utilized in the current research.

3. Results and discussion

In this section, a numerical study is presented, focusing on the process of natural convection melting within a trapezoidal enclosure. The unique aspect of this investigation lies in the utilization of non-Newtonian PCMs infused with MWCNT nanoparticles. The considered case is characterized by A Stefan number (*Ste*) of 0.16, a Rayleigh number (*Ra*) of 1.45×10^6, and a Prandtl number (*Pr*) of 51.7 for the host PCM. The study explores the impact of dispersing MWCNT nanoparticles within the PCM and varying the trapezoidal angle ($-\pi/6 \leq \gamma \leq +\pi/6$) on the melting process.

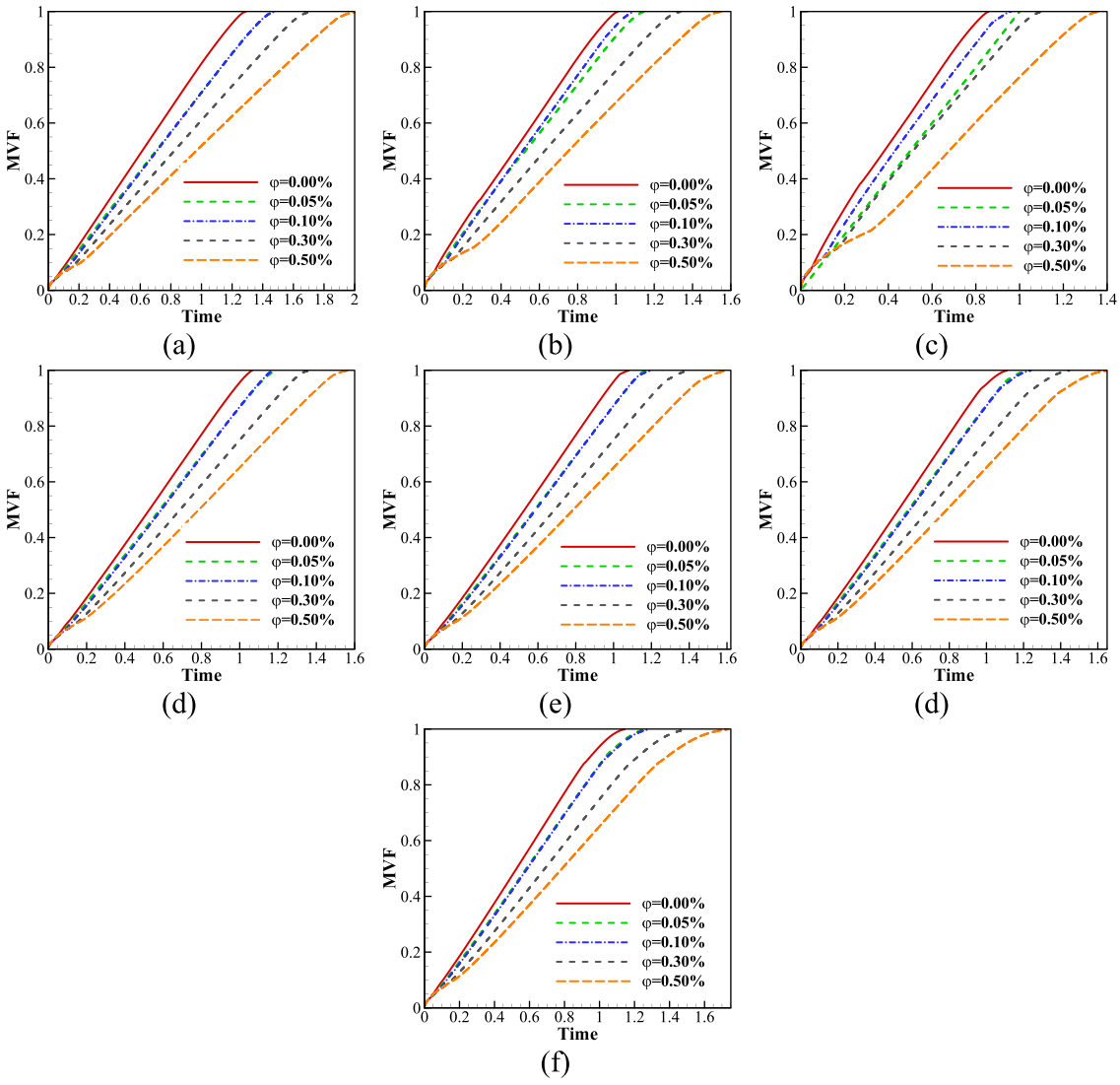

Fig. 12. MVF for different values of φ at (a) $\gamma = +30°$, (b) $\gamma = +20°$, (c) $\gamma = +10°$, (d) $\gamma = 0.0°$, (e) $\gamma = -10°$, (f) $\gamma = -20°$, and (g) $\gamma = -30°$.

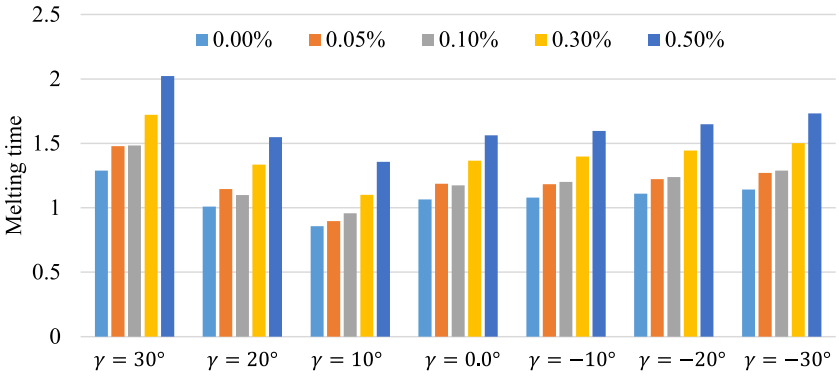

Fig. 13. Melting time for different cases.

The melting interface and velocity contours at various non-dimensional time steps and trapezoidal angles (γ) are depicted in Figs. 5-10. The presence of nanoparticles with a power law index lower than unity induces shear-thinning effects. At the same time, the concentration increase enhances the consistency parameter, equivalent to an increase in base viscosity. As the nanoparticles concentration rises, the initiation of natural convection circulations is delayed, as observed in Figs. 5 and 6. Without natural convection effects, the nano-PCM surrounding the element heats up, reducing temperature gradients and decreasing Nu_{avg}. However, when natural convection commences, the molten PCM transfers energy between solid and liquid phases, leading to substantial temperature gradients and enhanced heat transfer rate near the hot wall. Interestingly, Nu_{avg} reaches a lower steady level as the nanoparticle concentration increases, attributed to the shear-thinning

effects reducing the interaction of liquid PCM with the heated surface, resulting in smaller temperature gradients and heat transfer rates.

Towards the end of the melting process (Fig. 11(a)), Nu_{avg} exhibits a drop first for $\varphi = 0\%$, followed by $\varphi = 0.1\%$ and $\varphi = 0.5\%$, as each case reaches full melt consecutively. Finally, the temperature of the liquid PCM smoothly reaches the temperature of the hot wall, with energy storage occurring primarily in the form of sensible heat.

Fig. 5 provides valuable insights into the characteristics of the melting interface during the final stages of the melting process (non-dimensional time $\sim$ 1.0). A notable observation is that the melting interface appears sharp for the case of $\varphi = 0\%$, while it exhibits a more rounded shape for $\varphi = 0.1\%$ and $\varphi = 0.5\%$.. This difference can be attributed to the enhanced shear-thinning effects resulting from the increase in nanoparticle concentration. The shear-thinning behavior reduces the surface shear rate at the melting interface, resulting in a smoother and more rounded surface than the sharp interface observed in the absence of nanoparticles.

Figs. 7 and 8 present the melting interface and velocities within a right-angle enclosure ($\gamma = 0°$), which exhibits similar characteristics to the trapezoidal case. Rising the concentration of nanoparticles declines the melting fraction and delays the melting process. Moreover, the rise in nanoparticle concentration delays the initiation of natural convection circulations. However, in the case of $\gamma = 0°$, the melting process occurs much faster than in the previous case ($\gamma = 30°$). The straight walls of the enclosure play a crucial role in guiding the streamlines and enhancing the natural convection circulations. The streamlines demonstrate the initiation of natural convection flow in the middle of the heated surface, moving upward until the heated molten PCM reaches the top solid PCM. Subsequently, it releases its heat to the solid PCM and cools down. The cooled liquid PCM then flows along the side of the solid PCM, reaching the bottom wall to be heated once again. The shape of the solid-liquid PCM near the bottom indicates that the liquid PCM turns upward just before reaching the hot surface. This is due to a strong upward hot flow that counteracts the cold flow in that region.

Figs. 9 and 10 showcase the melting interface and streamlines within a trapezoidal enclosure with $\gamma = -30°$, where the walls are inclined inward. In this configuration, the melting process initiates from the hot bottom wall and gradually spreads in a circular pattern. Due to the inward inclination of the walls, the melting region swiftly reaches the side walls. The top corner edges are particularly exposed to the convection flows and easily undergo melting. In contrast, in the case of outward side walls ($\gamma = 30°$), as depicted in Figs. 5 and 6, the top corners trap the molten liquid and prove challenging to melt. The contrasting behavior between the inward and outward-inclined walls highlights the significant influence of enclosure geometry on the melting dynamics and the subsequent distribution of the molten liquid.

Figs. 11 and 12 present the time history of the average Nusselt number and melt fraction for different concentrations of nanoparticles and trapezoidal angles, respectively. Specifically, Fig. 11(a) showcases the time history of Nu_{avg} for five nanoparticle concentrations (0%, 0.05%, 0.1%, 0.3%, and 0.5%) at a trapezoidal angle of 30°, along with the corresponding melting fraction shown in Fig. 12(a). The results indicate that an increase in nanoparticle concentration leads to a delay in the melting process. Notably, Nu_{avg} initially decreases, then sharply rises to a high value, and eventually tends to remain constant for an extended period before sharply reducing at the end of the melting process. The increase in nanoparticle concentration prolongs the declining period due to the non-Newtonian behavior of the PCM in the presence of nanoparticles.

Fig. 13 compares the melting times for different trapezoidal angles and nanoparticle concentrations. Among the investigated cases, the shortest melting time is observed for $\gamma = 10°$ and $\varphi = 0\%$ with a time of approximately 0.75. In contrast, the longest melting time is found for $\gamma = 30°$ and $\varphi = 0.5\%$ with a time of around 2. Thus, the variation in trapezoidal angle and nanoparticles concentration can result in a 62.5% change in the melting time. When considering a fixed trapezoidal angle of $\gamma = 30°$, the shortest melting time is approximately 1.6 ($\varphi = 0\%$), while the longest time is around 2.0. Therefore, the melting time can vary by 20% for this particular geometry. Generally, a trapezoidal enclosure with a small outward angle ($\gamma = 0°$) yields the best results. In this case, the walls minimize interference with the streamlines, and the top corners exhibit a reduced tendency to trap solid PCM and streamlines. Consequently, this configuration offers the shortest melting time compared to the other investigated cases.

4. Conclusions

The study explored the non-Newtonian melting of NEPCM consisting of MWCNT particles in a trapezoidal enclosure using an enthalpy-porosity grid-fixed approach. The focus was the influence of MWCNT nanoparticle concentrations on the thermophysical properties of the nanocomposites based on PCM OM08-MWCNTs in both solid and liquid states.

In this investigation, a trapezoidal enclosure was filled with these nanocomposites, and the effects of different nanoparticle concentrations and trapezoidal angles were analyzed. The study shed light on the critical influence of enclosure geometry on the melting dynamics and heat transfer process. The key outcomes can be summarized as follows:

- Higher concentrations of nanoparticles introduced a delay in the initiation of natural convection circulations and resulted in an overall delay in the melting process. Although using MWCNTs improved the thermal conductivity of NePCMs, they increased the overall dynamic viscosity and deteriorated the natural convection heat transfer, leading to a low heat transfer rate.
- Varying the trapezoidal angle ($-\pi/6 \leq \lambda \leq +\pi/6$) significantly affected the melting dynamics and distribution of the molten liquid. The shortest melting time was found in a trapezoidal enclosure with a small outward angle ($\gamma = 0°$), indicating the role of geometry in the phase transition process.
- The melting interface changes shape based on nanoparticle concentration: a sharp interface for the case of 0% concentration, while more rounded for 0.1% and 0.5% concentrations due to enhanced shear-thinning effects.
- With increased nanoparticle concentration, the Nusselt number (Nu_{avg}) initially decreases, then sharply rises to a high value, and eventually tends to remain constant before dropping sharply at the end of the melting process.
- Trapezoidal angle and nanoparticle concentration variations can lead to a 62.5% change in melting time. The shortest time for fixed $\gamma = 30°$ is $\varphi = 0\%$, with a 20% variation as the concentration rises to $\varphi = 0.5\%$. A trapezoidal enclosure with a small outward angle ($\gamma = 10°$) minimizes interference and yields the shortest melting time.

The present study indicated that the shape of the enclosure and the concentration of nanoparticles can notably impact the melting rate. Thus, future studies can focus on optimizing enclosure shapes and heating locations for maximum heat transfer enhancement.

CRediT authorship contribution statement

Mohamed Boujelbene: Conceptualization, Methodology, Writing – original draft, Writing – review & editing. **S.A.M. Mehryan:** Conceptualization, Supervision, Methodology, Software, Formal analysis, Data curation. **Amira M. Hussin:** Conceptualization, Validation, Investigation, Writing – original draft, Writing – review & editing. **Talal Yusaf:** Conceptualization, Software, Writing – original draft, Writing – review & editing. **Mohammad Shahabadi:** Investigation, Methodology, Writing – review & editing. **Mohammad Ghalambaz:** Supervision, Investigation, Writing – original draft, Methodology, Writing – review & editing.

Declaration of Competing Interest

The authors declare that they have no known competing financial interests or personal relationships that could have appeared to influence the work reported in this paper.

Data availability

No data was used for the research described in the article.

Acknowledgment

This study is supported via funding from Prince Sattam bin Abdulaziz University project number (PSAU/2023/R/1444).

References

[1] G. Sadeghi, Energy storage on demand: thermal energy storage development, materials, design, and integration challenges, Energy Stor. Mater. 46 (2022) 192–222.
[2] S. Zhang, P. Ocłoń, J.J. Klemeš, P. Michorczyk, K. Pielichowska, K. Pielichowski, Renewable energy systems for building heating, cooling and electricity production with thermal energy storage, Renew. Sust. Energ. Rev. 165 (2022) 112560.
[3] C. Xu, H. Zhang, G. Fang, Review on thermal conductivity improvement of phase change materials with enhanced additives for thermal energy storage, J. Energy Stor. 51 (2022) 104568.
[4] Z. Liu, S.-M. Huang, C. Wang, Y. Zhuang, A review on non-Newtonian effects and structure-activity relationship of nanoparticles enhanced phase change materials in porous media, J. Energy Stor. 64 (2023) 107221.
[5] M. Izadi, A. Hajjar, H.M. Alshehri, M. Sheremet, A.M. Galal, Charging process of a partially heated trapezoidal thermal energy storage filled by nano-enhanced PCM using controlable uniform magnetic field, Int. Commun. Heat Mass Transf. 138 (2022) 106349.
[6] N.S. Dhaidan, Nanostructures assisted melting of phase change materials in various cavities, Appl. Therm. Eng. 111 (2017) 193–212.
[7] S. Chatterjee, D. Bhanja, S. Nath, Numerical investigation of heat transfer and melting process of phase change material in trapezoidal cavities with different shapes and different heated tube positions, J. Energy Stor. 72 (2023) 108285.
[8] N.S. Dhaidan, A.F. Khalaf, J.M. Khodadadi, Numerical and experimental investigation of melting of paraffin in a hemicylindrical capsule, J. Therm. Sci. Eng. Appl. 13 (5) (2021), 051008.
[9] F. Ahmad, S. Hussain, I. Ahmad, T.S. Hassan, A.O. Almatroud, W. Ali, I.E. Farooq, Successive melting of a phase change material bounded in a finned trapezoidal domain, Case Stud. Therm. Eng. 28 (2021) 101419.
[10] N.S. Dhaidan, Thermal performance of constrained melting of PCM inside an elliptical capsule of two orientations, Iran. J. Sci. Technol. Trans. Mech. Eng. 45 (2021) 515–521.
[11] F. Iachachene, Z. Haddad, H.F. Oztop, E. Abu-Nada, Melting of phase change materials in a trapezoidal cavity: orientation and nanoparticles effects, J. Mol. Liq. 292 (2019) 110592.
[12] Z.H. Khan, W.A. Khan, M.A. Sheremet, M. Hamid, M. Du, Irreversibilities in natural convection inside a right-angled trapezoidal cavity with sinusoidal wall temperature, Phys. Fluids 33 (8) (2021).
[13] D. Cimpean, M. Sheremet, I. Pop, Mixed convection of hybrid nanofluid in a porous trapezoidal chamber, Int. Commun. Heat Mass Transf. 116 (2020) 104627.
[14] N. Gibanov, M.A. Sheremet, Effect of trapezoidal heater on natural convection heat transfer and fluid flow inside a cubical cavity, Int. J. Numer. Methods Heat Fluid Flow 29 (4) (2019) 1232–1248.
[15] M. Boujelbene, H.I. Mohammed, H.S. Majdi, R. Babaei-Mahani, P. Talebizadehsardari, A. Rahbari, Melting performance of nano-enhanced phase change materials in a triple-tube heat exchanger with zigzag-shaped tubes, J. Energy Stor. 67 (2023) 107484.
[16] N.B. Khedher, J.M. Mahdi, H.S. Majdi, W.K. Al-Azzawi, S. Dhahbi, P. Talebizadehsardari, A hybrid solidification enhancement in a latent-heat storage system with nanoparticles, porous foam, and fin-aided foam strips, J. Energy Stor. 56 (2022) 106070.
[17] N.B. Bondareva, Numerical simulation of natural convection melting in 2D and 3D enclosures, J. Therm. Eng. 5 (1) (2019) 51–61.
[18] S. Sabet, B. Buonomo, M.A. Sheremet, O. Manca, Numerical investigation of melting process for phase change material (PCM) embedded in metal foam structures with kelvin cells at pore scale level, Int. J. Heat Mass Transf. 214 (2023) 124440.
[19] Y. Zhuang, Z. Liu, W. Xu, Experimental investigation on the non-Newtonian to Newtonian rheology transition of nanoparticles enhanced phase change material during melting, Colloids Surf. A Physicochem. Eng. Asp. 629 (2021) 127432.
[20] M. Ghalambaz, S.M.H. Zadeh, S. Mehryan, K.A. Ayoubloo, N. Sedaghatizadeh, Non-Newtonian behavior of an electrical and magnetizable phase change material in a filled enclosure in the presence of a non-uniform magnetic field, Int. Commun. Heat Mass Transf. 110 (2020) 104437.
[21] S. Kebriti, H. Moqtaderi, Numerical simulation of convective non-Newtonian power-law solid-liquid phase change using the lattice Boltzmann method, Int. J. Therm. Sci. 159 (2021) 106574.
[22] A. Khan, R.A. Shah, M.K. Alam, H. Ahmed, M. Shahzad, S. Rehman, S. Ahmed, M. S. Khan, A.-H. Abdel-Aty, M. Zakarya, Computational investigation of an unsteady non-Newtonian and non-isothermal fluid between coaxial contracting channels: a PCM approach, Results in Physics 28 (2021) 104570.
[23] Y. Zhuang, J. Lin, A. Liu, Numerical investigation on non-Newtonian melting heat transfer of phase change material composited with nanoparticles and metal foam in an inner heated cubic cavity, J. Energy Stor. 51 (2022) 104417.
[24] Z. Haddad, F. Iachachene, M.A. Sheremet, E. Abu-Nada, Numerical investigation and optimization of melting performance for thermal energy storage system partially filled with metal foam layer: new design configurations, Appl. Therm. Eng. 223 (2023) 119809.
[25] C. Biserni, F. Dalpiaz, T. Fagundes, L. Rocha, Constructal design of T-shaped morphing fins coupled with a trapezoidal basement: a numerical investigation by means of exhaustive search and genetic algorithm, Int. J. Heat Mass Transf. 109 (2017) 73–81.
[26] R. da Silveira Borahel, F.S.F. Zinani, L.A.O. Rocha, E.D. dos Santos, L.A. Isoldi, C. Biserni, Geometric optimization of a rectangular isothermal block inside a lid-driven cavity by means of constructal design, Int. Commun. Heat Mass Transf. 139 (2022) 106499.
[27] G.V. Gonzales, C. Biserni, E. da Silva Diaz Estrada, G.M. Platt, L.A. Isoldi, L.A. O. Rocha, A.J. da Silva Neto, E.D. dos Santos, Investigation on the association of differential evolution and constructal design for geometric optimization of double Y-shaped cooling cavities inserted into walls with heat generation, Appl. Sci. 13 (3) (2023) 1998.
[28] E.H.T. Cunegatto, F.S.F. Zinani, C. Biserni, L.A.O. Rocha, Constructal design of passive micromixers with multiple obstacles via computational fluid dynamics, Int. J. Heat Mass Transf. 215 (2023) 124519.
[29] C. Yadav, R.R. Sahoo, Experimental analysis for optimum thermal performance and thermophysical parameters of MWCNT based capric acid PCM by using T-history method, Powder Technol. 364 (2020) 392–403.
[30] A.K. Gupta, G. Mishra, S. Singh, Numerical study of MWCNT enhanced PCM melting through a heated undulated wall in the latent heat storage unit, Therm. Sci. Eng. Progr. 27 (2022) 101172.
[31] M. AlOtaibi, M. Alsuhybani, M. Khayyat, B. AlOtaibi, Performance of nanocomposites of a phase change material formed by the dispersion of MWCNT/TiO2 for thermal energy storage applications, Materials 15 (9) (2022) 3063.
[32] M.A. Fikri, A. Pandey, M. Samykano, K. Kadirgama, M. George, R. Saidur, J. Selvaraj, N. Abd Rahim, K. Sharma, V. Tyagi, Thermal conductivity, reliability, and stability assessment of phase change material (PCM) doped with functionalized multi-wall carbon nanotubes (FMWCNTs), J. Energy Stor. 50 (2022) 104676.
[33] I. Chabani, F. Mebarek-Oudina, H. Vaidya, A. Ismail, Numerical analysis of magnetic hybrid Nano-fluid natural convective flow in an adjusted porous trapezoidal enclosure, J. Magn. Magn. Mater. 564 (2022) 170142.
[34] H. Shahzad, Q.U. Ain, A.A. Pasha, K. Irshad, I.A. Shah, A. Ghaffari, M.B. Hafeez, M. Krawczuk, Double-diffusive natural convection energy transfer in magnetically influenced Casson fluid flow in trapezoidal enclosure with fillets, Int. Commun. Heat Mass Transf. 137 (2022) 106236.
[35] S.C. Kim, R. Prabakaran, D. Sakthivadivel, N. Thangapandian, A. Bhatia, P. Ganesh Kumar, Thermal transport properties of carbon-assisted phase change nanocomposite, Fullerenes Nanotub. Carbon Nanostruct. 28 (11) (2020) 925–933.
[36] M. DASH, Blood Flow Dynamics on a Centrifugally Actuated Microfluidic Platform, Indian Institute of Technology, Kharagpur, 2014.
[37] Author Biography, in: O.C. Zienkiewicz, R.L. Taylor, P. Nithiarasu (Eds.), The Finite Element Method for Fluid Dynamics (Seventh Edition), Butterworth-Heinemann, Oxford, 2014, p. ii.
[38] J.C. De Los Reyes, S. González Andrade, A combined BDF-semismooth Newton approach for time-dependent Bingham flow, Numeri. Methods Partial Different. Equ. 28 (3) (2012) 834–860.
[39] O. Schenk, K. Gärtner, Solving unsymmetric sparse systems of linear equations with PARDISO, Futur. Gener. Comput. Syst. 20 (3) (2004) 475–487.
[40] P. Wriggers, Nonlinear Finite Element Methods, Springer Science & Business Media, 2008.
[41] F. Verbosio, A. De Coninck, D. Kourounis, O. Schenk, Enhancing the scalability of selected inversion factorization algorithms in genomic prediction, J. Comput. Sci. 22 (2017) 99–108.
[42] B. Kamkari, H. Shokouhmand, F. Bruno, Experimental investigation of the effect of inclination angle on convection-driven melting of phase change material in a rectangular enclosure, Int. J. Heat Mass Transf. 72 (2014) 186–200.
[43] B. Kamkari, H.J. Amlashi, Numerical simulation and experimental verification of constrained melting of phase change material in inclined rectangular enclosures, Int. Commun. Heat Mass Transf. 88 (2017) 211–219.